

# FURTHER RESULTS FROM A LABORATORY MODEL OF THE CONVECTIVE PLANETARY BOUNDARY LAYER

J. W. DEARDORFF and G. E. WILLIS

*Department of Atmospheric Sciences, Oregon State University, Corvallis, OR 97331, U.S.A.*

(Received 9 August, 1984)

**Abstract.** The turbulence in a laboratory convective mixed layer is probed more extensively than in the preliminary study of Willis and Deardorff (1974), and results presented. Turbulence intensities, spectra and probability distributions using mixed-layer scaling compare favorably with similarly scaled field measurements not available or plentiful in 1974. However, the velocity spectra in the convection tank exhibit only a short inertial subrange due to the close proximity of the dissipation subrange to the energy-containing range.

The turbulence budget suggests that the convergence of the vertical transport of pressure fluctuations is a rather important term.

Results on the entrainment rate are also presented, using both mixed-layer scaling and local interfacial scaling.

## 1. Introduction

Ten years ago the first laboratory results on turbulence structure in an entraining, convective boundary layer appeared (Willis and Deardorff, 1974, here called W&D). Their main value was to demonstrate the use of convective mixed-layer scaling whereby heights are normalized by the mean boundary-layer depth  $\bar{h}$ , turbulent velocities by the convective velocity scale,  $w_*$ , and temperature fluctuations in the lower boundary layer by the temperature scale  $T_* = \overline{w'T'_s}/w_*$ , where  $\overline{w'T'_s}$  is the surface kinematic heat flux. In the atmosphere, these quantities have typical magnitudes (in the daytime, over land) of 1 km,  $1.8 \text{ m s}^{-1}$ , and  $0.1^\circ\text{C}$ , respectively. They are often found within a factor of two of these values. By using laboratory apparatus in which  $\bar{h}$  is a few thousand times smaller and  $w_*$  a few hundred times smaller, the validity of convective mixed-layer scaling therefore could be more convincingly demonstrated than by using atmospheric data alone.

The main constraints are that  $\bar{h}$  in the laboratory model be sufficiently great that the turbulence Reynolds number be in the 'large' category so that its value is irrelevant, and that in atmospheric applications the inequality  $-\bar{h}/L \gg 1$  be satisfied, where  $L$  is the Obukhov length. The first constraint ensures that properly scaled turbulence values from the laboratory model do not depend on molecular properties (especially since the convection tank utilizes water instead of air). The second ensures that, except in the lowest part of the surface layer, the source of the atmospheric boundary-layer turbulence is primarily buoyant convection (especially since the laboratory tank has no mean shear).

The laboratory model is further restricted to apply only to atmospheric situations of flat terrain of nearly uniform surface temperature, fair-weather conditions free of

mesoscale disturbances, and absence of strong baroclinity or wind shear at  $z = \bar{h}$ . An additional limitation not well fulfilled in our 1974 studies is that the aspect ratio of convective-tank sidewall separation to  $\bar{h}$  be large. The side-wall separation is 1.24 m, which is only about twice the value of  $\bar{h}$  then utilized. Since then, smaller values of  $\bar{h}$  have been used, giving an aspect ratio of 5 or 6, while apparently maintaining a sufficiently large Reynolds number for many applications. One of the purpose of this paper is to document the changes in turbulence intensity associated with this improvement, and to compare the new vertical profiles with field measurements not available or relevantly scaled ten years ago.

The laboratory model has also been applied to single-particle diffusion studies (e.g., see Willis and Deardorff, 1976, 1981) and lately toward estimation of concentration fluctuations (Deardorff and Willis, 1984) whose analysis often involves two-particle separation statistics. For the latter purpose, the velocity spectra should be known in order to check that an inertial subrange exists at relevant scales. Accordingly, another purpose of this paper is to present velocity spectra and autocorrelations at various heights within the mixed layer. It will be found that only a very short inertial subrange exists in the laboratory tank, and an analysis will be presented on how much greater  $\bar{h}$  would need to be to extend the subrange by one decade.

The spectra allow estimates of the dissipation rate which are also presented along with proportionality constants involved in their parameterization. The turbulence kinetic energy budget in all but the lower 20% of the mixed layer is also presented, giving evidence that the pressure-fluctuation transport term tends to cancel at least half of the turbulent transport term, except in the entrainment layer.

Probability distributions for the velocity components and temperature at various heights relative to  $\bar{h}$  are also presented, as well as the  $w' - T'$  joint probability distribution. Finally, entrainment rates scaled with different length and velocity scales are presented for a narrow range of stabilities.

## 2. Experimental Methods

The laboratory tank is the same one used by W&D and is 1.24 m on a side. In the present experiments it is filled up to 0.4 m with filtered, degassed water, initially at 20 °C below 0.20 m and 32.5 °C above. After a few hours, molecular diffusion plus initial turbulence when filling the tank lead to a nearly constant stratification of 0.58 °C/cm<sup>-1</sup> between heights of 0.17 m and 0.24 m. After heating is applied to the bottom of the tank, this stratification is present just above the top of the mixed-layer into which the latter grows through entrainment. The upper water surface of the tank, at a height of  $\approx 0.35$  m, is kept covered as far as possible with large slabs of floating styrofoam so that evaporative cooling is minimized.

The vertical thermal structure is estimated from thermocouple measurements taken near the center of the tank. The thermocouple is traversed vertically at frequent intervals at a speed of 1.2 cm s<sup>-1</sup>. A second stationary thermocouple always located within the mixed layer allows a smoothed estimate of  $\partial T_m / \partial t$  to be made, where  $T_m$  is mean

mixed-layer temperature (corresponding to potential temperature in the atmosphere). From this record, the mean surface kinematic heat flux  $\overline{w'T'_s}$  is obtained:

$$\overline{w'T'_s} = (\bar{h}/1.2) \partial T_m / \partial t.$$

where the factor of 1.2 approximately accounts for the entrainment warming contribution (Deardorff *et al.*, 1980). Bottom-plate temperature was obtained with a thermocouple located within the aluminum tank bottom. During an experiment, it typically exceeded  $T_m$  by 10 °C.

The uppermost height of a mixed-layer dome ( $h_2$ ) located anywhere within the tank at any given time is obtained from the height of a horizontally spread laser beam projected horizontally across the tank. The index of refraction variations associated with the tops of mixed-layer domes are then clearly visible. From additional experiments when the mixed-layer contained dye, the height  $\langle h \rangle$  was taken as the height at which mixed-layer fluid occupies half the horizontal area (Deardorff *et al.*, 1980). (The angular brackets refer to the horizontal average; the overbar refers to the ensemble average along the traverse line.) Average values of  $h_2 - \langle h \rangle$  as a function of time were then obtained ( $h_2 - \langle h \rangle$  averaged 3 cm), and applied to  $h_2(t)$  from individual experiments to yield  $\langle h \rangle(t)$  from the individual experiments. From these data, the entrainment rate,  $\partial \langle h \rangle / \partial t$ , was also obtained.

A horizontal traversing mechanism mounted just above the tank top held an X-configuration hot-film anemometer (HFA) and an additional thermocouple whose tip was positioned 0.5 cm away from the center of the X (though much farther away in about half of the experiments). The downward extending support rods were 0.46 and 0.32 cm in diameter, respectively. The HFA sensed the two velocity components,  $u$  and  $w$ , with a superimposed traversing speed of 7.1 cm s<sup>-1</sup>. The sensor height could be varied between 4 and 28 cm. Much effort went into reducing the mechanical noise associated with the traversing – a fly wheel had to be installed on the motor drive shaft, vibrations of towing wires and from nearby pumps had to be suppressed, the traversing guide track across which the HFA supporting structure slid had to be kept continually oiled, and inertial weights had to be added to the HFA support structure.

A two-point HFA horizontal velocity calibration was performed a few minutes prior to each experiment, using traversing speeds of 5 and 9 cm s<sup>-1</sup>. The calibration determined the constants  $a$  and  $b$  in the usual formula for each of the two hot-film sensor responses:

$$E^2 = (a + bV_e^{0.33})(T_w - T) \quad (1)$$

where  $E$  is the HFA output voltage,  $V_e$  is the velocity component normal to the sensor cylinder,  $T_w$  is the hot-film temperature and  $T$  the water temperature. The value of the exponent, 0.33, was determined from more comprehensive calibrations; its precise value is not critical once  $a$  and  $b$  are determined accurately for each hot film.

$V_e$  was related to the true flow speed,  $V$ , and the angle of attack,  $\alpha$ , in the  $x - z$  plane by a relation investigated by Champagne *et al.* (1967):

$$V_e^2 = (1/2)V^2[(1 \mp \sin 2\alpha) + m^2(1 \pm \sin 2\alpha)] \quad (2)$$

where the  $\pm$  sign refers to one or the other of the two hot films, each inclined  $45^\circ$  from the horizontal. The quantity  $m$ , which empirically accounts for cooling due to a flow component parallel to the hot-film cylinder, was given the value 0.2 as recommended by Andreas (1973) for TSI hot film sensors of the type used here.

From (2),  $V$  is obtained from

$$V^2(1 + m^2) = V_{e1}^2 + V_{e2}^2 \quad (3)$$

and  $\alpha$  from

$$[(1 - m^2)/(1 + m^2)] \sin 2\alpha = (V_{e2}^2 - V_{e1}^2)(V_{e1}^2 + V_{e2}^2) \quad (4)$$

where subscripts 1 and 2 refer to the two respective hot films, and  $V_{e1,2}$  are obtained from (1). Finally,  $u$  and  $w$  are obtained from

$$u = V \cos \alpha$$

$$w = V \sin \alpha.$$

The effect of ambient temperature fluctuations upon  $u'$  was accounted for through direct use of (1) for experiments where  $T$  and HFA sensors were close together, and by an indirect statistical method in the other cases. Values of  $T_w - T$  in (1) averaged  $40^\circ\text{C}$ .

In an additional test performed just before the calibration runs of each experiment, the HFA is traversed at  $7.1 \text{ cm s}^{-1}$  and the noise levels in the  $u$  and  $w$  variances obtained, as well as any apparent mean offsets in  $u$  and  $w$ . These noise levels are later subtracted from the respective velocity component variances gathered when the thermal convection is present.

In any given experiment, 8 or 10 horizontal traverses with the HFA and thermocouple could be obtained before  $h$  grew too large (beyond about 0.24 m), allowing about 10 s recovery time between the end of a 'retrieval' traverse and the next 'data' traverse. Each traverse line was 0.84 m long, with data from it fed into a microcomputer at 20 ms intervals, corresponding to a distance increment of 1.4 mm. There were 9 experiments in which data were collected between heights of about 0.2 and  $1.0 \bar{h}$ , 3 additional experiments for which the collection heights were between 0.4 and  $1.0 \bar{h}$ , and 5 additional ones with excessive noise at the higher frequencies which could be used nevertheless in examining spectra in the energy-containing range and the short inertial subrange. In two further experiments, data were collected only in the  $0.8$  to  $1.14 \bar{h}$  height interval.

### 3. Results

#### 3.1. TEMPERATURE PROFILES AND THE HEAT FLUX

Thermocouple temperature profiles from one particular experiment are shown in Figure 1. These profiles were taken in the upward progressing direction so that after convection commenced at time  $t = 0$ , they exhibit a tendency for slightly excessive stability within the mixed-layer due to its continual warming. During the profiles at

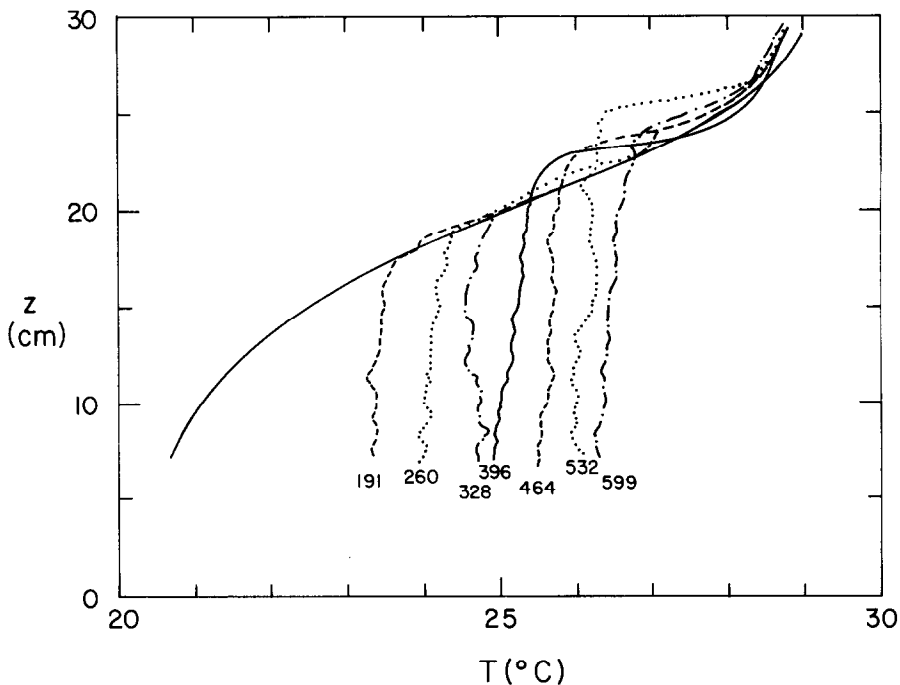


Fig. 1. Vertical profiles of temperature from an (upward) traversing thermocouple near the center of the convection tank. Numbers indicate time in seconds following initiation of convection in this particular experiment.

$t = 396, 464,$  and  $532$  s, it may be noted that a dominant thermal penetration or dome at the top of the mixed-layer existed at the thermocouple location. Due to such sampling variations, the heat flux was not obtained from the temperature profiles, but from  $w'$  and  $T'$  correlation measurements.

The ensemble-average values of  $\overline{w'T'}$ , relative to the surface flux, and grouped into 8 height levels, are shown in Figure 2. At the lowest height level, the magnitude was increased by 10%, and at the other levels by 5%, in a rough correction for sensor separation based upon autocorrelations to be presented later.

The right-hand scale is height,  $z$ , relative to  $\langle h \rangle$  obtained from the spread laser beam and representative of the convection tank as a whole. In the left-hand scale,  $\bar{h}$  has been decreased by 13% so that the most negative heat flux occurs where  $z/\bar{h} = 1$ , as found to hold approximately by Deardorff *et al.* (1980). This 13% discrepancy between the two dimensionless height scales indicates that the particular traverse line utilized in the tank measurements was not fully representative of the tank's entire horizontal area. A discrepancy of this sense had been suspected before the measurement series was completed, and 4 final experiments with dye in the mixed-layer confirmed that the level of 50% dye coverage along the traverse line tended to be some 2 cm lower than the equivalent height based on the horizontal average. Later, the probable cause was traced to collection of rust in some of the spray-pipe holes in the heat exchanger underneath

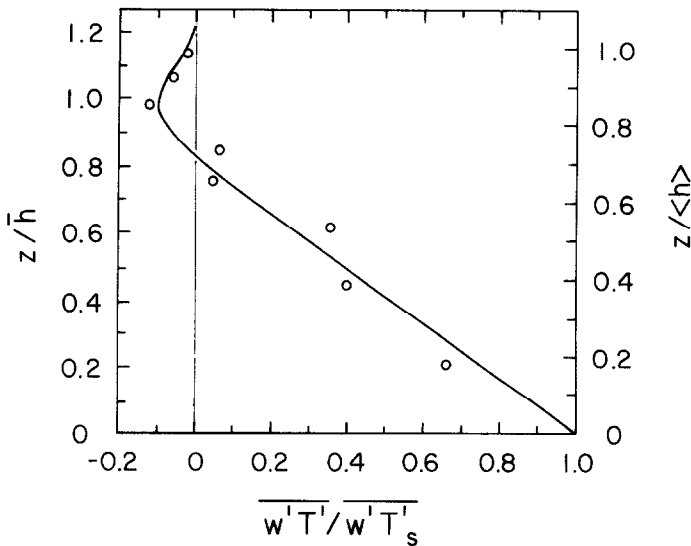


Fig. 2. Vertical profiles of turbulent heat flux,  $\overline{w'T'}$ , relative to the surface flux, from correlation measurements of  $w'$  and  $T'$ . Right-hand ordinate,  $z/\langle h \rangle$ , refers to relative height within the convection tank as a whole; left-hand ordinate,  $z/\bar{h}$ , refers to height of measurements relative to  $h$  along the single horizontal traversing line.

the aluminum tank bottom. As a result, the bottom-plate root-mean-square temperature fluctuation, in the horizontal, was found to average 4.5% of the mean surface-to-bulk temperature drop rather than the 1.3% figure in the earlier experiments of W&D. In this respect, the laboratory situation had become analogous to that in the field, where the mean mixed-layer height deduced from aircraft flights along some given flight path is likely to differ by  $\pm 15\%$  from that deduced from an areal lidar measurement over a larger region, and where surface temperature variations may not be entirely negligible.

A linear extrapolation of the heat-flux profile from the lowest 2/3 of the mixed-layer to  $z/\bar{h} = 1$  produces an 'entrainment-flux' value that is 0.2 of the surface flux. The same approximate ratio was obtained in previous measurements of W&D and Deardorff (1979), with the most negative heat flux actually being substantially less than this value.

The problem of determining a simple, reliable parameterization for the surface heat flux under conditions of vanishingly small mean flow is still not satisfactorily solved. We know of no better relation than that of Townsend (1964):

$$\overline{w'T'_s} = C(g\beta\kappa^2/\nu)^{1/3}(\Delta T_b)^{3/2} \quad (5)$$

where  $g$  is the gravitational acceleration,  $\beta$  the coefficient of thermal expansion,  $\kappa$  and  $\nu$  the molecular diffusivities of heat and momentum,  $\Delta T_b$  the temperature difference between the bottom surface and the bulk fluid near the middle of the mixed-layer, and  $C$  is a constant. It was found that  $C = 0.14$  during the first 10% of the measurement period, declining to 0.10 by the end. Similar behavior was noted by Deardorff *et al.* (1969) where  $C$  declined from about 0.24 to 0.20 during the same time period. The

reason for the smaller value of  $C$  here than in those experiments or in Townsend's (1964) experiment where  $C = 0.19$  is not known. Presumably the decline of  $C$  with time indicates a deficiency of (5). The more favorable horizontal aspect ratio in the present experiments might be thought to be a causal factor, but the decline in  $C$  as this aspect ratio becomes less favorable (as  $\bar{h}$  grows during an experiment) does not support this possibility.

#### VARIANCES OF $u$ , $w$ , $T$

The variance of the horizontal velocity component, or  $\overline{u'^2}$ , normalized by  $w_*^2$ , is shown in Figure 3 by the solid curve. The error bars denote the standard error of the mean

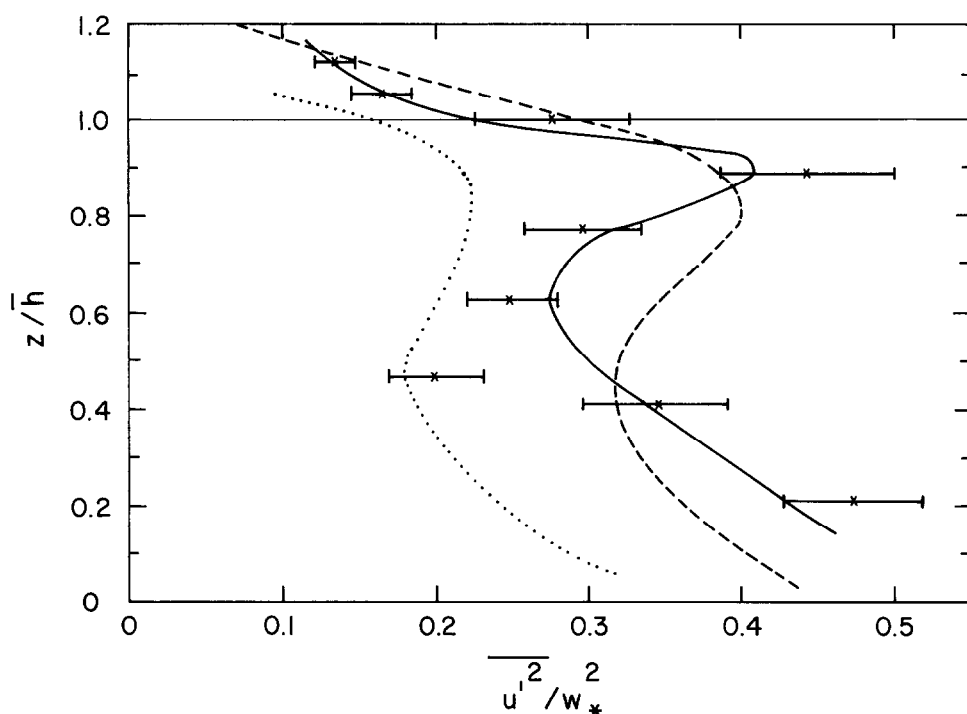


Fig. 3. Vertical profile of a horizontal velocity-component variance,  $\overline{u'^2}$ , normalized by  $w_*^2$ . x's and solid curve through (most of) the error bars (standard error of the mean): present hot-film anemometer measurements; dotted curve: laboratory measurements of W&D (1974); dashed curve: field measurements reported by Caughey (1982).

estimate; i.e., 67% of the time one would expect a smooth mean curve to pass within the error bars. These variances include the largest scale of circulation possible – an eddy of the same sign along the whole length of the HFA traversing line – since the true ensemble horizontal mean ( $\langle u \rangle = 0$ ) was known. This large-scale contribution to the total variance typically averaged 17%. Also shown is the profile from Caughey (1982) from the 1973 Minnesota experiment and the 1976 Ashchurch experiment combined,

and the profile from W&D. In comparison with the latter, the increased values of the present set of experiments seem to be due to the greater horizontal spacing between side walls relative to the eddy length scale, or to  $\bar{h}$ . The (rough) overall agreement with Caughey's (1982) data suggests that, in the absence of appreciable mesoscale forcing, the horizontal velocity variance is primarily associated with scales of convective motion of  $6\bar{h}$  and less.

Values of  $w_*$ ,  $T_*$  and  $\bar{h}$  associated with these measurements, and with spectra to be presented, are given in Table I. They vary somewhat with the different relative heights

TABLE I  
Convection parameters

$z/\bar{h}$	$w_*$ (cm s <sup>-1</sup> )	$T_*$ (C)	$\bar{h}$ (m)	No. of spectra or prob. dists. entering average
0.21	0.76	0.11	0.189	18
0.40	0.73	0.094	0.199	16
0.48	0.83	0.14	0.169	17
0.62	0.75	0.10	0.193	15
0.79	0.83	0.14	0.170	23
0.89	0.75	0.10	0.196	14
0.99	0.76	0.10	0.197	10
1.06	0.79	0.13	0.187	19
1.14	0.79	0.14	0.161	33

of measurement because the surface heat flux typically increased slightly at first during an experiment then declined,  $\bar{h}$  always gradually increased, and the 4 to 5 different heights of measurement below  $z = \bar{h}$  were cycled twice in a top-to-bottom direction.

The variance of the vertical velocity,  $\overline{w'^2}$ , normalized by  $w_*^2$ , is shown in Figure 4. Again there is rough agreement with Caughey's (1982) data although our maximum value occurs somewhat lower, near  $z/\bar{h} = 0.4$ . The decreased values in comparison with W&D supports the interpretation that in those experiments sidewall confinement caused an underemphasis in the horizontal components and an overemphasis in the vertical component of motion. The same conclusion had previously been reached by Ferreira (1977) from data also in Adrian and Ferreira (1979). The surface-layer curve of Wyngaard *et al.* (1971) is also shown in Figure 4 but is an overestimate above the surface layer.

The temperature variance,  $\overline{T'^2}$ , relative to  $T_*^2 = (\overline{w'T'_s}/w_*)^2$  is shown in Figure 5. The present values are seen to agree more closely with those of Caughey (1982) than with those of W&D in the lower half of the mixed-layer. It is not clear if or why the improved horizontal aspect ratio is responsible for this better agreement. In the upper part of the boundary layer, it is known that  $\overline{T'^2}$  is dominated by influences of the mixed-layer capping inversion,  $\Delta T$  (Wyngaard and LeMone, 1980), which in turn depends on factors other than  $T_*$ ,  $w_*$  and  $\bar{h}$ . Thus simple mixed-layer scaling does not work in that region.



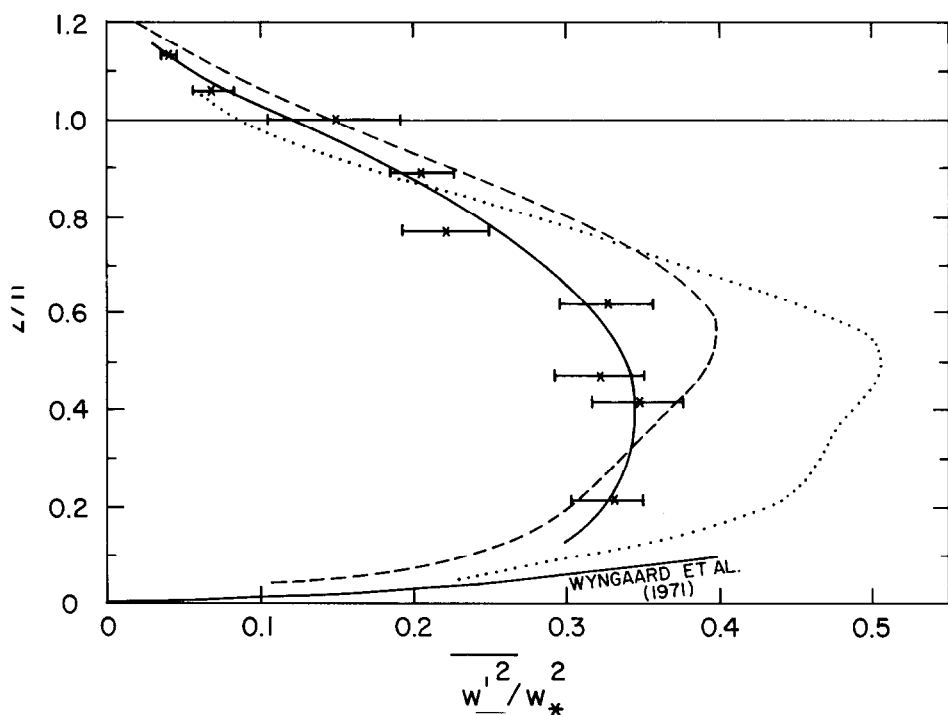


Fig. 4. Vertical profile of vertical-velocity variance,  $w'^2$ , normalized by  $w_*^2$ . x's and solid curve through error bars: present results; dotted curve: W&D; dashed curve: Caughey (1982); lowest solid curve: surface-layer free-convection relation of Wyngaard *et al.* (1971).

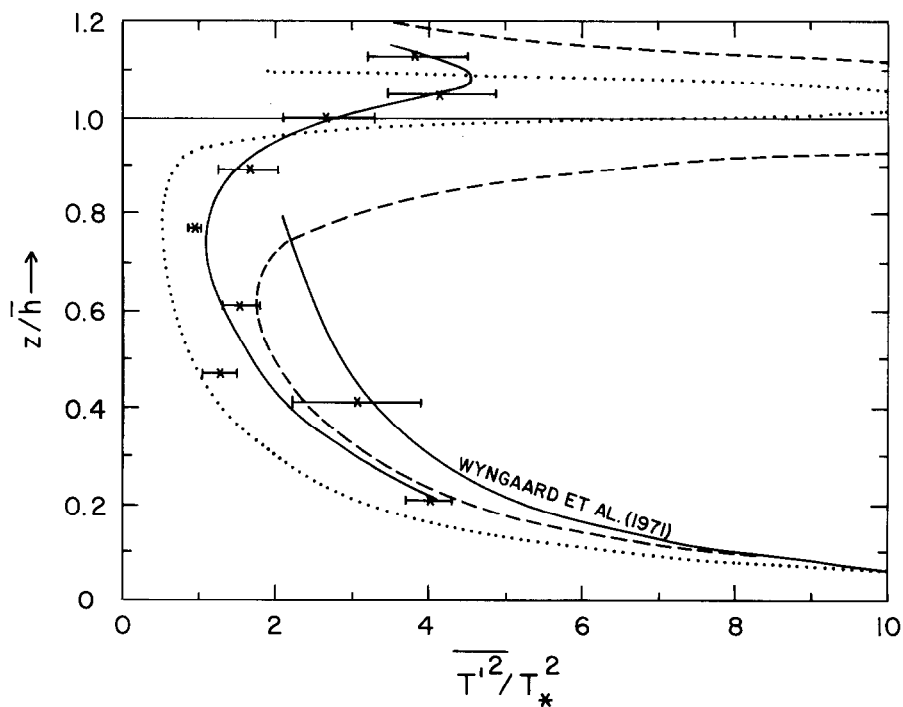


Fig. 5. Vertical profile of temperature variance normalized by  $T_*^2$ . x's and solid curve through error bars: present results; dotted curve: results of W&D; dashed curve: Caughey (1982); right-hand solid curve: surface-layer free-convection relation of Wyngaard *et al.* (1971).

### 3.3. HORIZONTAL SPECTRA

One-dimensional spectra along the HFA traversing line were obtained by the fast-Fourier transform for 512 points, starting 0.23 m from one wall and ending 0.15 m from the opposite wall. The data preconditioning involved the quadratic tapering of the first and last 5% of the data along each line so that end points would match. Typically, about 2% of the variance was lost by this process.

The spectra  $\Phi$  for  $w$  are shown in Figure 6 in the energy-conserving type of plot wherein the ordinate is  $k\Phi_w(k)$  normalized by  $w_*^2$ , where  $k$  is the wavenumber. On the abscissa, the inner and upper scale is  $L_x/\bar{h}$ , where  $L_x$  is the wavelength along  $x$  given by  $L_x = 2\pi/k$ ; it increases to the left. The bottom abscissa is  $k\bar{h}$  which increases to the right as customary. For  $L_x/\bar{h} < 0.3$ , the spectra are averages over wavenumber bands,  $\Delta k$ , such that  $\Delta k/k \simeq 0.2$ . The Nyquist frequency corresponds to  $L_x/\bar{h} \simeq 0.016$ .

The spectra of Figure 6(a) are seen to exhibit the inertial subrange slope ( $-2/3$ ) for  $0.7 > L_x/\bar{h} > 0.15$ . For  $L_x/\bar{h} < 0.1$ , the effect of molecular dissipation causes the spectra to begin their downward plunges. For  $L_x/\bar{h} < 0.03$ , the effect of noise dominates – noise associated with traversing the HFA and with other tank vibrations. The noise appears to become significant actually for  $L_x/\bar{h} \simeq 0.06$ . The noisy portions of these spectra are only included as a reminder of the frequency response available and of the serious difficulties in obtaining velocity spectra when the sensor must be traversed. Noise was also a problem in the free-convection spectra of Ferreira (1978) who used a traversing laser doppler velocimeter.

For  $L_x/\bar{h} > 0.15$ , these  $k\Phi_w(k)$  spectra agree quite closely with those of Kaimal *et al.* (1976) for their height category of  $0.2 < z/\bar{h} < 1$  (upon multiplying their values by  $\psi^{2/3} = 0.71$ ). Their maximal values of  $k\Phi_w(k)/w_*^2$  then ranged between 0.065 and 0.10 while our maxima, if similarly smoothed, range between 0.06 and 0.12. Their smoothed maxima occurred for  $L_x/\bar{h}$  between 1.0 and 1.5, while ours in the same height range occur for  $L_x/\bar{h}$  between 1 and 2. Although these maxima in  $k\Phi_w(k)$  occur at larger wavelengths as  $z/\bar{h}$  increases to 1, we see a suggestion in Figure 6(c) for a shift back to smaller wavelengths for  $z/\bar{h}$  between 1 and 1.2.

Although the vertical error bars would admit considerable uncertainty in the placement of mean curves, such curves do not appear to show any statistically significant small-scale distinct peaks. The minor peaks that are seen to occur are about what are expected due to data randomness and finite sampling. Thus our  $w$  spectra do not suggest that the dominant or organized thermal structures exhibit any particular peak that distinguishes them from the rest of the turbulence. Apparently their somewhat variable sizes and shapes, especially their random positions with respect to the sampling line, preclude this. However, Grossman's (1982) moderately convective over-ocean cases did tend to show a separate peak for  $L_x/\bar{h} = 2.4$ , followed by a dip at shorter wavelengths. This feature occurred in both alongwind and crosswind cases, and was considered significant. Grossman (1982) refers to Ivanov (1970) for qualitatively similar spectral behavior, from overland tower data. However, overland aircraft measurements of  $\Phi_w$  by Lenschow (1970) also do not show any isolated peaks of statistical significance.

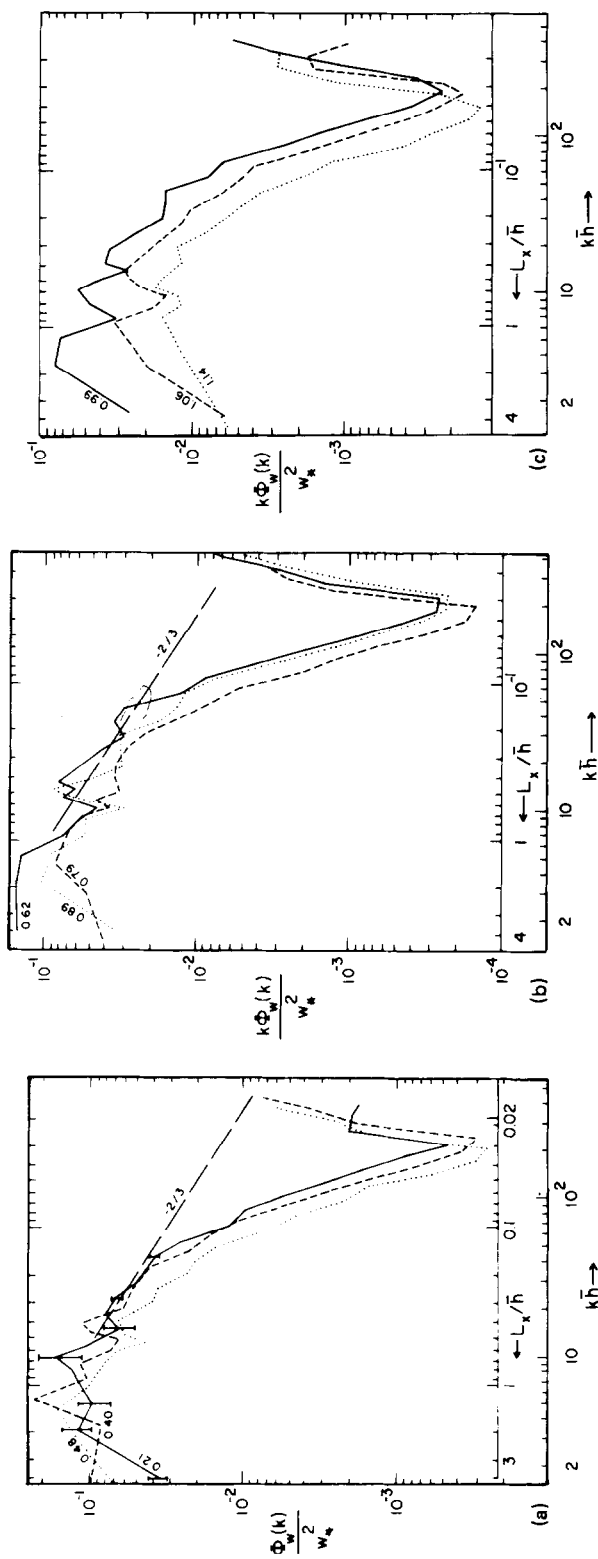


fig. 6. Vertical velocity ( $w$ ) spectra in energy-conserving format versus  $L_x/\bar{h}$  (inner and upper abscissae) and  $k\bar{h}$  (lowest abscissa). For  $z/h$  values of: (a) 0.21, 0.40 and 0.48 as labelled; (b) 0.62, 0.79 and 0.89; and (c) 0.89, 1.06, and 1.14.

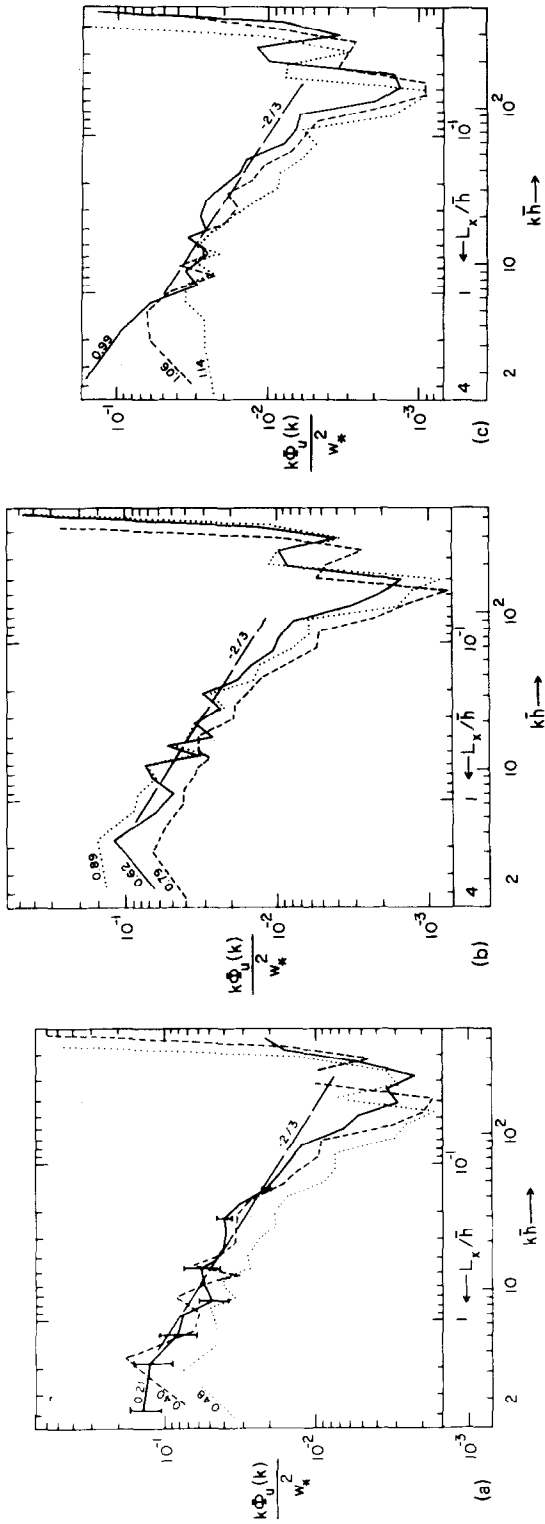


Fig. 7. Horizontal velocity-component ( $u$ ) spectra in energy-conserving format versus  $L_x/\bar{h}$  and  $k\bar{h}$ . See also Figure 6 caption.

The  $u$  spectra,  $k\Phi_u(k)$  in Figure 7, also exhibit a short section of inertial subrange behavior, for  $0.7 < L_x/\bar{h} < 0.2$ , merging smoothly into the rest of the energy containing range on the left and the dissipation range on the right. The noise-level problem was even more severe with  $u$  than with  $w$  because the translation axis coincides with the  $u$ -component direction. In addition, the noise pulse occurring at  $L_x/\bar{h} = 0.08$  can be explained as due to the shedding frequency of Kármán vortices from the HFA support rod.

The temperature spectra,  $k\Phi_T(k)$ , in Figure 8 are normalized by  $T_*^2$ . Interestingly, they exhibit relatively constant values at all heights in the wavenumber band where the velocities showed inertial-subrange behavior. A Batchelor (1959) viscous-convective subrange ( $-1$  slope on a  $\Phi_T(k)$  log-log plot or 0 slope here) is to be expected in a fluid of large Prandtl number such as water, where  $\nu/k \simeq 7$ . However, it is expected to commence to the right of the inertial subrange. Here, the Batchelor subrange seems to be superimposed over the inertial-subrange position. This odd behavior deserves further study, and may somehow be associated with the near proximity of the dissipation subrange to the energy-containing range. The phenomenon must be related to a similar result in a study by Grant *et al.* (1968) that the Batchelor  $-1$  spectrum in water commences not at the wavenumber where the (velocity) inertial subrange ends, but at a wavenumber about 4 times smaller. The phenomenon is not of direct interest to boundary-layer meteorologists, especially since the atmospheric Prandtl number (0.7) is not large.

The temperature spectra display a strong noise peak at a frequency of about twice that of the  $u$ -component Kármán-vortex peak, and was found to be associated with the close proximity of the hot-film sensor to the thermocouple. The temperature spectrum obtained at  $z/\bar{h} = 0.1$  in Deardorff and Willis (1982), in which no HFA was used, closely resembles the present one at  $z/\bar{h} = 0.2$  if this noise spike is removed.

### 3.4. AUTOCORRELATIONS

The self-correlations of  $u$ ,  $w$ , and  $T$  along  $x$  were obtained numerically from smoothed versions of the spectra with the noise subjectively removed, using the fast-Fourier transform of the spectral density.

The autocorrelation for  $w$ , defined by

$$r_w = \overline{w(x)w(x + \delta x)} / w'^2$$

is shown in Figure 9 at the height  $z/\bar{h} = 0.21$  by the solid curve as a function of the dimensionless separation  $\delta x/\bar{h}$ . Since the spectrum from which it was obtained contains only periodic components, it turns out that the integral scale as customarily defined would be identically zero. Here, attention will therefore be given to the length scale at which  $r(\delta x)$  drops to  $1/e$  and the scale at which it first crosses zero, respectively.

Due to the absence of an extended inertial subrange and the resolution of much of the dissipation range, the curvature in  $r_w$  near the origin (Taylor, 1935) is apparent in the right-hand portion of Figure 9. The dashed curve is the  $w$  autocorrelation which results if the inertial subrange is artificially extended but all longer-wavelength modes

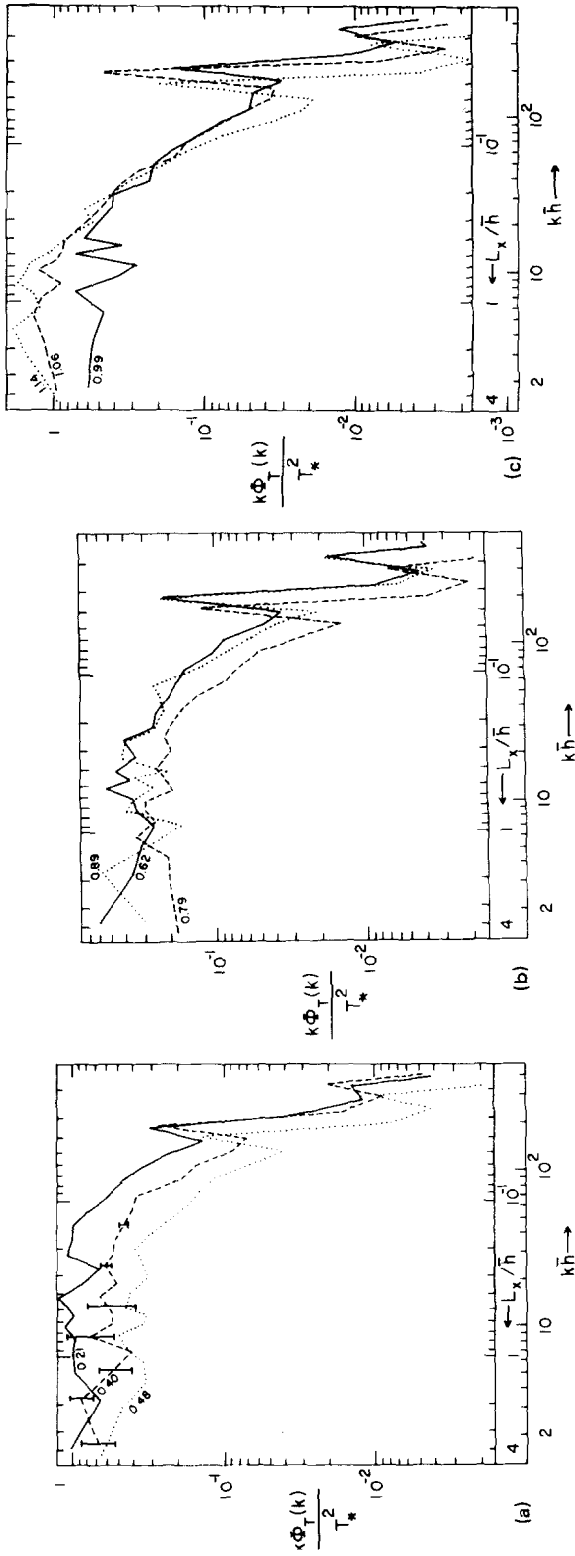


Fig. 8. Temperature ( $T$ ) spectra versus  $L_x/\hbar$  and  $k\hbar$ . See also Figure 6 caption.

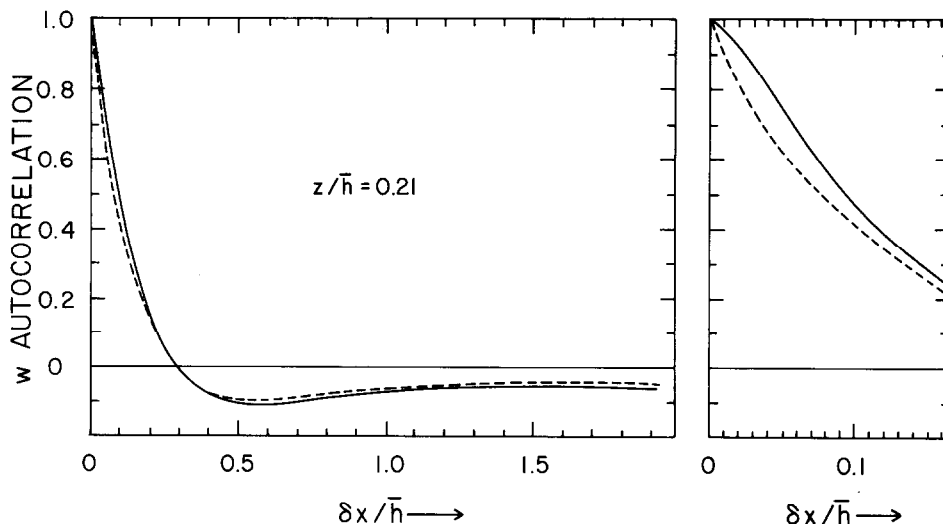


Fig. 9. Vertical-velocity autocorrelation versus horizontal separation ( $\delta x$ ) normalized by  $\bar{h}$ , for  $z/\bar{h} = 0.21$ . Solid curve from present results; dashed curve derived from smoothed spectrum modified to have an extended inertial subrange. Right-hand frame is same as left frame but with an expanded abscissa.

left unchanged. It appears much more exponential in shape near the origin. However, there is only a 12% overestimate in the  $1/e$  length scale due to the absence of an extended inertial subrange in the tank, and no change in the zero-crossover scale. We thus consider the laboratory convection tank to be a useful tool for estimating these length scales.

For  $z/\bar{h} = 0.21$ , our laboratory curve for  $r_w$  for  $\delta x/\bar{h} < 0.17$  is closely approximated by

$$r_w = \exp - (\delta x/\bar{h})/[0.1 + 0.003/(\delta x/\bar{h})]. \quad (6)$$

The  $r_w$  curves for all heights sampled are shown in Figure 10(a-c) and for  $u$  and  $T$  in Figures 11 and 12, respectively. There is a large change to greater scales in moving upwards 0.2 units from  $z/\bar{h} = 0.21$ , and presumably a continuing trend to smaller scales if descending below 0.21. In the central mixed-layer, however, from  $0.4 < z/\bar{h} < 0.7$ , the autocorrelation curves for  $w$  are quite similar, though above  $z/\bar{h} = 0.6$  they fall off more rapidly upon moving farther upwards. These trends are shown in Figure 13 (solid curves) for the  $1/e$  and zero-crossover scales, respectively.

As could be expected from the different properties of tangential and normal velocity components, the  $u$  autocorrelations do not show the rapid change at lower heights which  $r_w$  displays; see Figure 11(a-c). The biggest changes occur within the upper entrainment zone where the length scales become smaller, as seen also in Figure 13. The apparent decline in both the  $u$  and  $w$  length scales at the top of the mixed layer suggests that in this region they are not entirely governed by the mixed-layer depth,  $\bar{h}$ , but perhaps also by the thickness of the entrainment zone. For applications within the latter zone, however, the scales might still be considered proportional to  $\bar{h}$ , given the proper

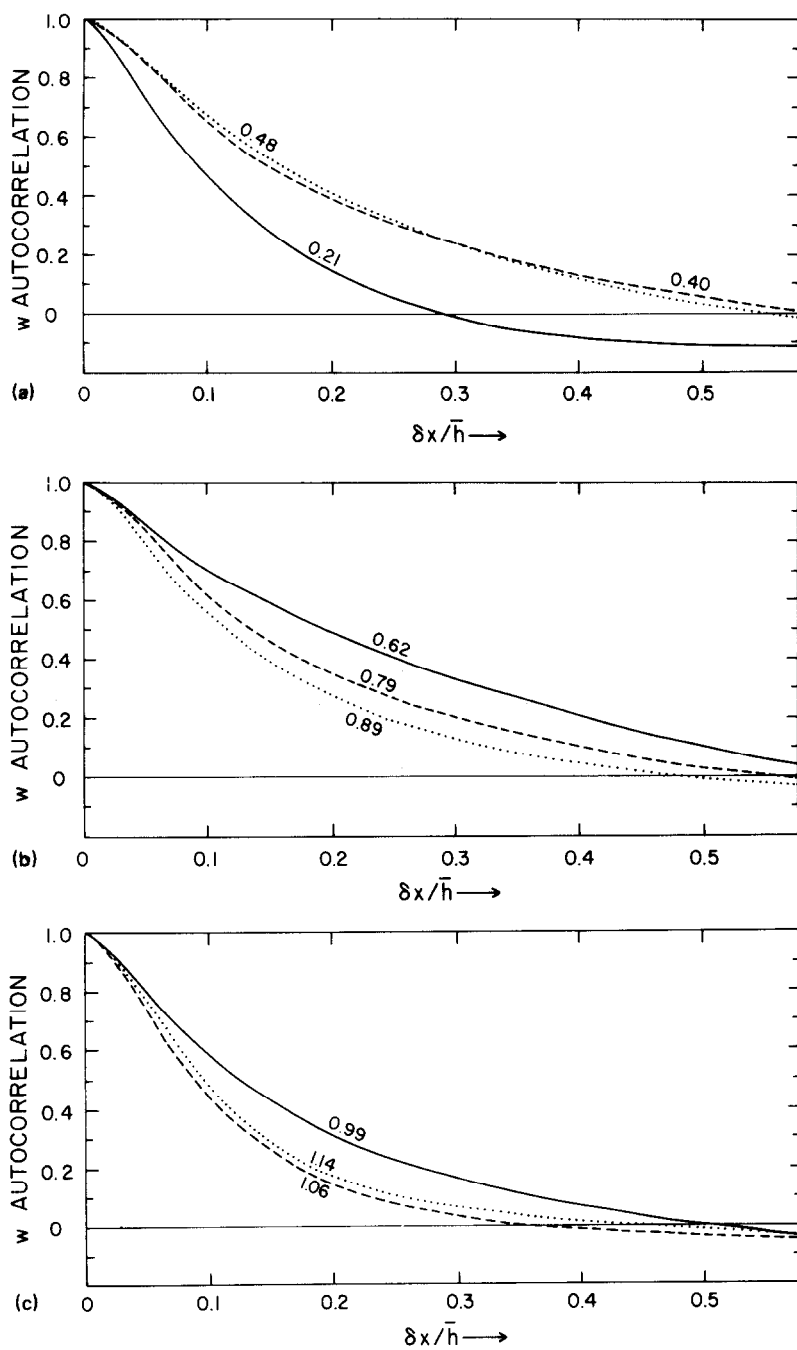


Fig. 10.  $w$  autocorrelation versus  $\delta x / \bar{h}$  for  $z / \bar{h}$  values of: (a) 0.21, 0.40, and 0.48 as labelled; (b) 0.62, 0.79 and 0.89; and (c) 0.99, 1.06 and 1.14.



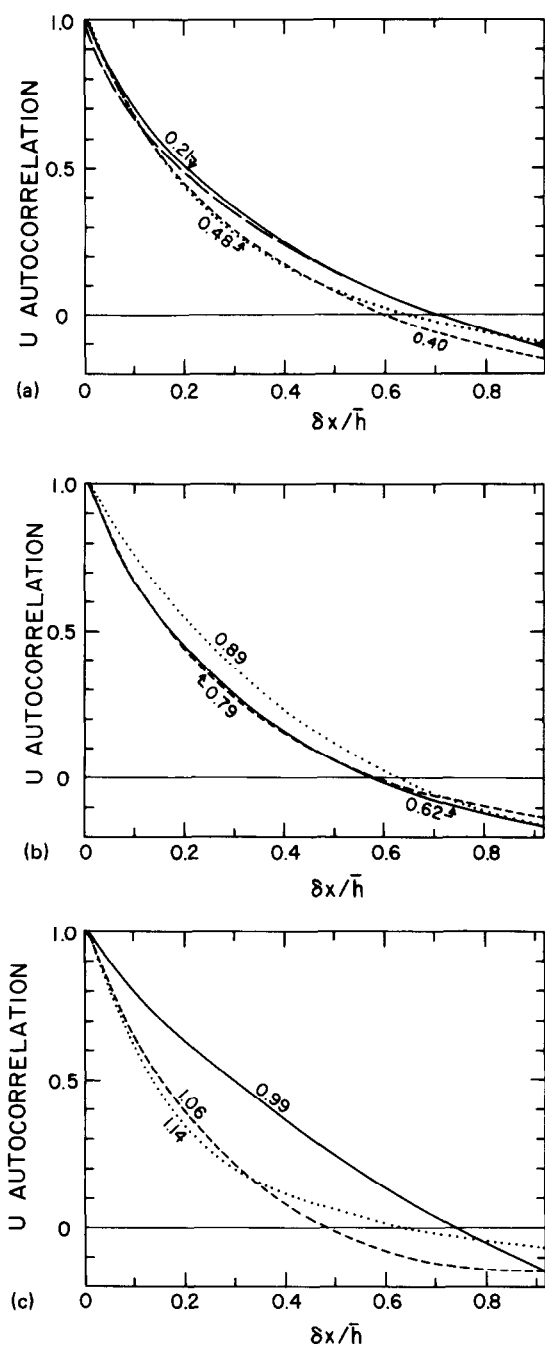


Fig. 11.  $u$  autocorrelations versus  $\delta x / \bar{h}$ . See also Figure 10 caption. Long-dash curve in (a) is from smoothed  $u$  spectrum at  $z/\bar{h} = 0.21$  modified to have an extended inertial subrange.

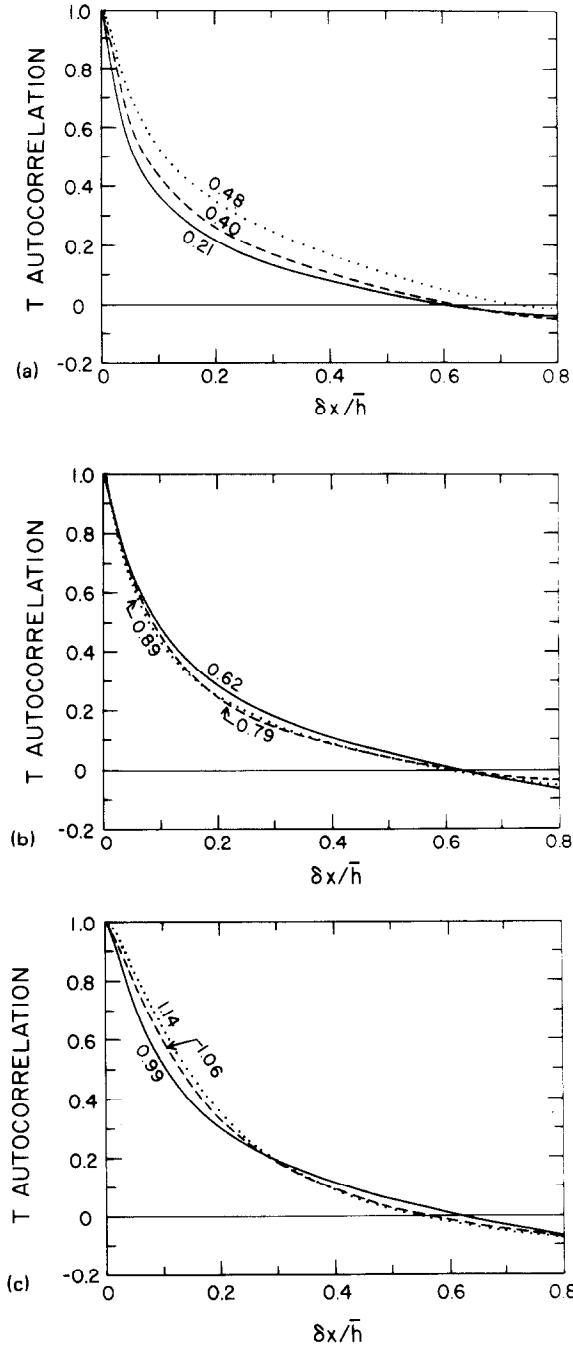


Fig. 12.  $T$  autocorrelations versus  $\delta x / \bar{h}$ . See also Figure 10 caption.

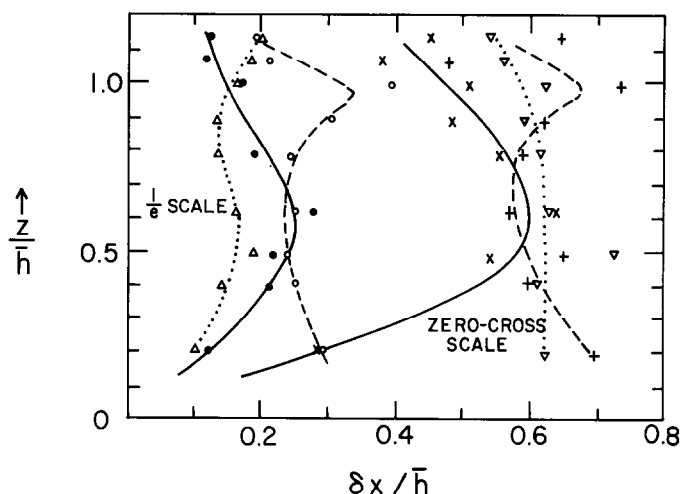


Fig. 13. Vertical profiles of  $1/e$  autocorrelation fall-off scales (left-hand group) and zero-crossover scales (right-hand group) for  $w$  (solid curves and closed circles or  $x$ 's); for  $u$  (dashed curves and open circles or  $+$ ); and for  $T$  (dotted curves and upright or inverted triangles).

proportionality constant. This topic is discussed further by Zeman and Tennekes (1977).

The autocorrelation curves for temperature, Figure 12, behave rather intermediate to those of  $r_w$  and  $r_u$ . As seen in Figure 13,  $r_T$  somewhat more closely resembles  $r_w$  out to the  $1/e$  scale, but more closely resembles  $r_u$  at the zero-crossover scale.

### 3.5. THE TURBULENCE KINETIC ENERGY (TKE) BUDGET

The terms in the TKE budget are

$$\begin{aligned} (1/)(\partial/\partial t)(\overline{u'^2} + \overline{v'^2} + \overline{w'^2}) = & \underbrace{g\beta \overline{w'T'}}_I - \underbrace{\varepsilon}_{II} - \underbrace{(\partial/\partial z) [\overline{w'(u'^2 + v'^2 + w'^2)/2}]}_{III} - \\ & - \underbrace{(\partial/\partial z) (\overline{w'p'/\rho})}_{IV} \end{aligned} \quad (7)$$

where term I is the buoyancy production; term II is the dissipation rate,  $\varepsilon$ ; term III is the TKE transport convergence; and term IV is the pressure-transport convergence. The left-hand side of (7) is negligible here, so that term IV can be treated as a residual upon estimating terms I, II, and III. Term I is available from Figure 2. The terms to be presented have been made dimensionless by dividing (7) by  $w_*^3/\bar{h}$ .

Term II was estimated from the direct viscous relation, assuming isotropy on small scales, of

$$\varepsilon = (15/2) \nu (\partial w / \partial x)^2. \quad (8)$$

In obtaining  $\overline{(\partial w / \partial x)^2}$ , the  $w$  spectra of Figure 5 were used, after smoothing and continuing the high-frequency fall-off with noise removed. The negative of term II then

becomes

$$\bar{\varepsilon}\bar{h}/w_*^3 = (15/2) \left( \frac{\nu}{w_*\bar{h}} \right) \int_0^\infty [k\Phi_w(k)/w_*^2] (k\bar{h})^2 d(\ln k\bar{h}). \quad (9)$$

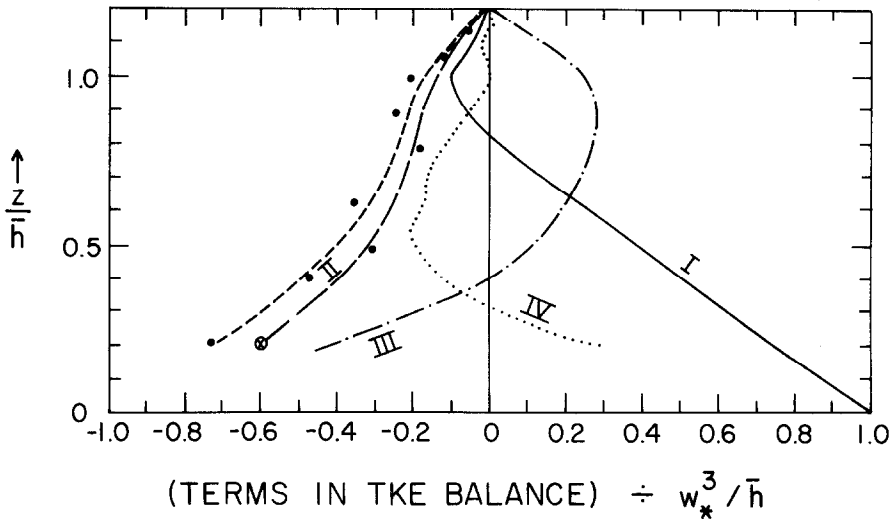


Fig. 14. Turbulence kinetic energy balance, normalized by  $w_*^3/\bar{h}$ , versus  $z/\bar{h}$ . Curve I (solid) is buoyant production; curve II (right-hand dashed curve of the pair) is dissipation; curve III (dash-dot) is convergence of  $w'e'$ ; curve IV (dotted) is the residual (pressure transport, hopefully).

Data-point values of term II are shown in Figure 14 by dots through which the left-most smooth curve has been subjectively drawn. The  $u$  spectra were not additionally used in estimating  $\varepsilon$  because the noise level for those data commenced at too low a frequency.

The existence of apparent inertial subranges (though short) in the  $u$  and  $w$  spectra allowed further estimates of term II from

$$\bar{\varepsilon}\bar{h}/w_*^3 = (0.50 C')^{-3/2} k\bar{h} [k\Phi(k)/w_*^2]^{3/2} \quad (10)$$

where 0.50 is the inertial subrange constant for  $u$  along  $x$ , and  $C' = 1$  therefore when  $\Phi = \Phi_u$  and  $C' = 4/3$  for  $\Phi = \Phi_w$ . However, the use of (10) was considered sufficiently valid only for the lowest height which exhibited the best developed inertial subrange. The average of the two values obtained at this height from (10) using  $u$  and  $w$  spectra is shown in Figure 14 by the encircled  $x$ . It is considered more reliable than the estimate from (9) since, for one reason, isotropy did not hold on these scales so close to the energy-containing range. Therefore, the curve from (9) was corrected at all heights by multiplying it by the ratio (0.82) derived from utilizing (10) at the lowest height. The resulting long-dash curve on the left in Figure 13 was then used in the TKE budget.

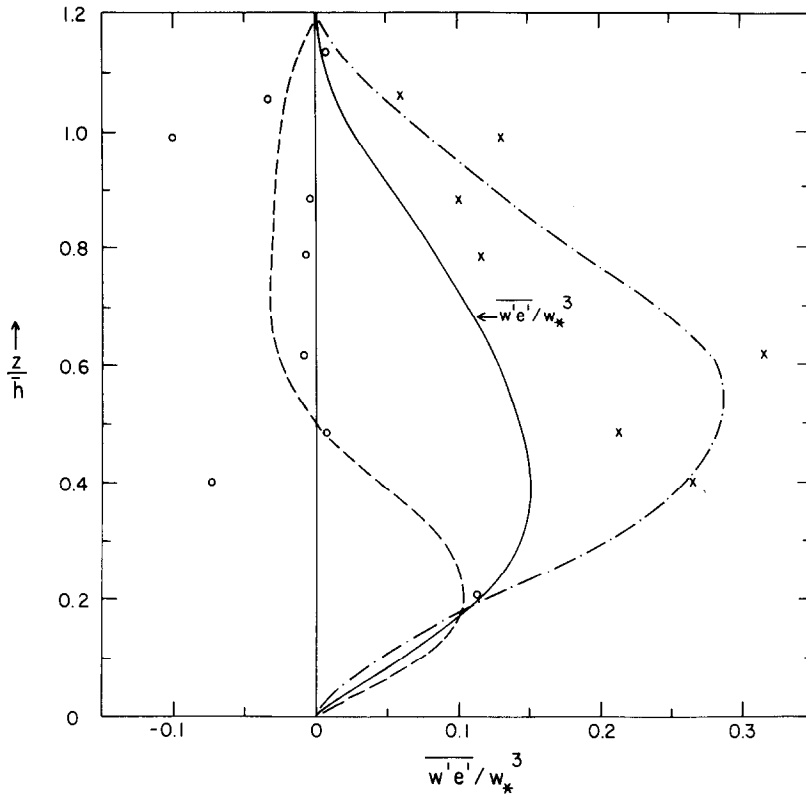


Fig. 15. Vertical profiles of:  $\overline{w'e'}/w_*^3$  (solid curve);  $\overline{w'^3}/w_*^3$  (dash-dot curve drawn by hand through data-point x's); and  $2\overline{w'u'^2}/w_*^3$  (dashed curve and circle data points). Curves are extrapolated below  $z/\bar{h} = 0.2$ .

Term II was obtained by differentiation of the highly smoothed curve for  $\overline{w'e'}/w_*^3 = (\overline{w'^3} + 2\overline{w'u'^2})/(2w_*^3)$  shown in Figure 15. The individual contributions from  $\overline{w'^3}$  and  $2\overline{w'u'^2}$  are also shown. The latter data points exhibited sufficient scatter that a zero value at all heights could almost have been assumed. However, our  $\overline{w'e'}$  curve turned out to be virtually identical to that of Druilhet and Durand (1984).

The overall budget appears somewhat more realistic than in D&W where term IV had been considered minor and had been lumped in with the dissipation. In fact, the sum of terms II and IV here closely resembles its average counterpart in W&D. The dissipation in Figure 14 decreases somewhat more with height within the bulk of the mixed-layer than in W&D or in Lenschow (1970). This decrease seems mostly realistic since the horizontal scales of  $w$  decrease rapidly with height progressing downwards below  $z/\bar{h} \simeq 0.25$ . Our present values of dimensionless dissipation are similar to those of Guillemet *et al.* (1983) which lay near 0.65 at  $z/\bar{h} = 0.2$  and decreased to about 0.25 at  $z/\bar{h} = 1$ . The present TKE balance agrees well with that of Lenschow *et al.* (1980) except that term IV here does not become positive again in the upper mixed layer. Uncertainty in either term II or III, or both, might be responsible. However, a reasonable

extrapolation of term IV downward will yield a zero vertical integral, which provides a gross though weak check on the overall reliability of the budget. Although term IV may seem to compensate a surprisingly large fraction of term III, the former was estimated to be larger still in magnitude in a convective surface layer studied by Caughey and Wyngaard (1979).

### 3.6. DISSIPATION PARAMETERIZATION

A commonly used parameterization for  $\varepsilon$  is

$$\varepsilon = c(\text{TKE})^{3/2}/l \quad (11)$$

where TKE is the turbulence kinetic energy,  $c$  is a constant and  $l$  is a macro length scale. There are many possible definitions for  $l$ , usually involving the integral length scale or its close relative, the  $1/e$  autocorrelation fall-off scale. Here  $l$  is defined as

$$l = (l_u l_v l_w)^{1/3} \quad (12)$$

where  $l_u = l_v$  is the  $1/e$  length scale for  $u$  along  $x$ , and  $l_w$  is the same for  $w$  along  $x$ . With this definition and the use of Figures 3, 4, 13, and 14, it is found that  $c$  in (11) has an average value at the 9 height levels of  $c = 0.24 \pm 0.02$ , where the uncertainty again represents the standard error of the mean. If  $l$  is redefined as  $(l_u l_w)^{1/2}$ , the result becomes  $c = 0.23 \pm 0.02$ .

In comparison, for neutral stratification Dickey and Mellor (1980) found  $c = 0.61$ . The model tested by Hassid and Galperin (1983), upon utilizing  $l \simeq 0.23 \bar{h}$  as in Figure 13, gives  $c = 0.14$  within the bulk of a convectively mixed-layer above the surface layer, upon further assuming that the TKE is constant with height.

### 3.7. WHAT SIZE TANK FOR AN EXTENDED INERTIAL SUBRANGE?

If the inertial subrange were artificially extended by one decade, followed by a dissipation-range spectral shape identical to those of Figure 5 with noise removed, one may use (9) to calculate how  $v/(w_* \bar{h})$  would have to be altered so that  $\varepsilon \bar{h}/w_*^3$  on the left side would remain the same to balance the TKE budget. (Only a slight downward adjustment in overall spectral energy level would be needed to compensate for the increased TKE added by the inertial subrange extension.) When this exercise was done, it was found that the dimensionless dissipation would be much too great unless  $v/(w_* \bar{h})$  were 53 times smaller. Holding the surface heat flux per unit area the same, this would require  $\bar{h}$  to be 20 times larger. Thus,  $\bar{h}$  would need to be about 4 m, requiring sidewall separations of about 20 m: in effect, a deep swimming pool would be needed with bottom heating-rate energy requirements several hundred times greater than for our laboratory tank. Such requirements are prohibitive, but indicate that in a shallow buoyancy-driven oceanic mixed-layer of a few meters depth (a rarity), the inertial subrange would not be very extensive.

### 3.8. PROBABILITY DISTRIBUTIONS

The probability,  $P_w$ , of occurrence of  $w/w_*$  within the increment  $\Delta w/w_*$  is presented in Figure 16 for the nine levels of measurement. It is normalized such that

$$\int_{-\infty}^{\infty} P_w dw/w_* = 1. \quad (13)$$

Before plotting, some of the curves were shifted slightly horizontally to ensure that the ensemble average of  $w$  at any level,  $\bar{w}$ , was zero. That is, the condition

$$\int_{-\infty}^{\infty} (\bar{w}/w_*) P_w d\bar{w}/w_* = 0 \quad (14)$$

was enforced because small mean values of  $\bar{w}$  existed but would vanish in the absence of sampling error and instrumental error. The average magnitude of the corrective shift was  $0.047 w/w_*$  units. From these curves, the  $\overline{w'^3/2}$  contribution to Figure 15 was obtained from

$$(1/2) \overline{(w/w_*)^3} = (1/2) \int_{-\infty}^{\infty} (w/w_*)^3 P_w dw/w_*. \quad (15)$$

The expected skewness in  $w$  is evident from Figure 16, though it disappears at heights above  $z/\bar{h} = 0.9$ . It should be noted that the present  $w/w_*$  data categories (with  $\Delta w/w_* = 0.13$ ) did not extend quite far enough towards positive values at some heights. In those cases, the final value on the right may show an upturn, as it includes within the category all higher-amplitude  $w$  occurrences.

We did not find the most probable negative value of  $w/w_*$  to be as large as did Lamb (1982) utilizing data from large-eddy numerical simulations in three dimensions. See Figure 16(a, b) for Lamb's (1982) probability values for  $z/\bar{h} = 0.25$  and  $0.75$ , respectively. The inherent uncertainties in both methods of estimation of  $P_w$  do not allow us to conclude which (if either) is the more correct. Our measurements probably suffer more from sampling error than did Lamb's data, especially since our measurement line was found to be somewhat non-representative of the convection tank as a whole. On the other hand, the numerically derived data contain errors of unknown magnitude associated with subgrid-scale flux approximations and truncation error. However, the tails of the two independently derived probability distributions agree remarkably well, and both show the skewness decreasing with height. The  $P_w$  distributions of Caughey *et al.* (1983) for  $z/\bar{h} = 0.42$  agree better with the Lamb (1982) data values than with the present ones, while at greater heights they agree very well with the present ones.

The probability distributions for the horizontal velocity component appeared relatively Gaussian and are not presented here.

The probability distributions for temperature,  $P_T$ , are shown in Figure 17. Below

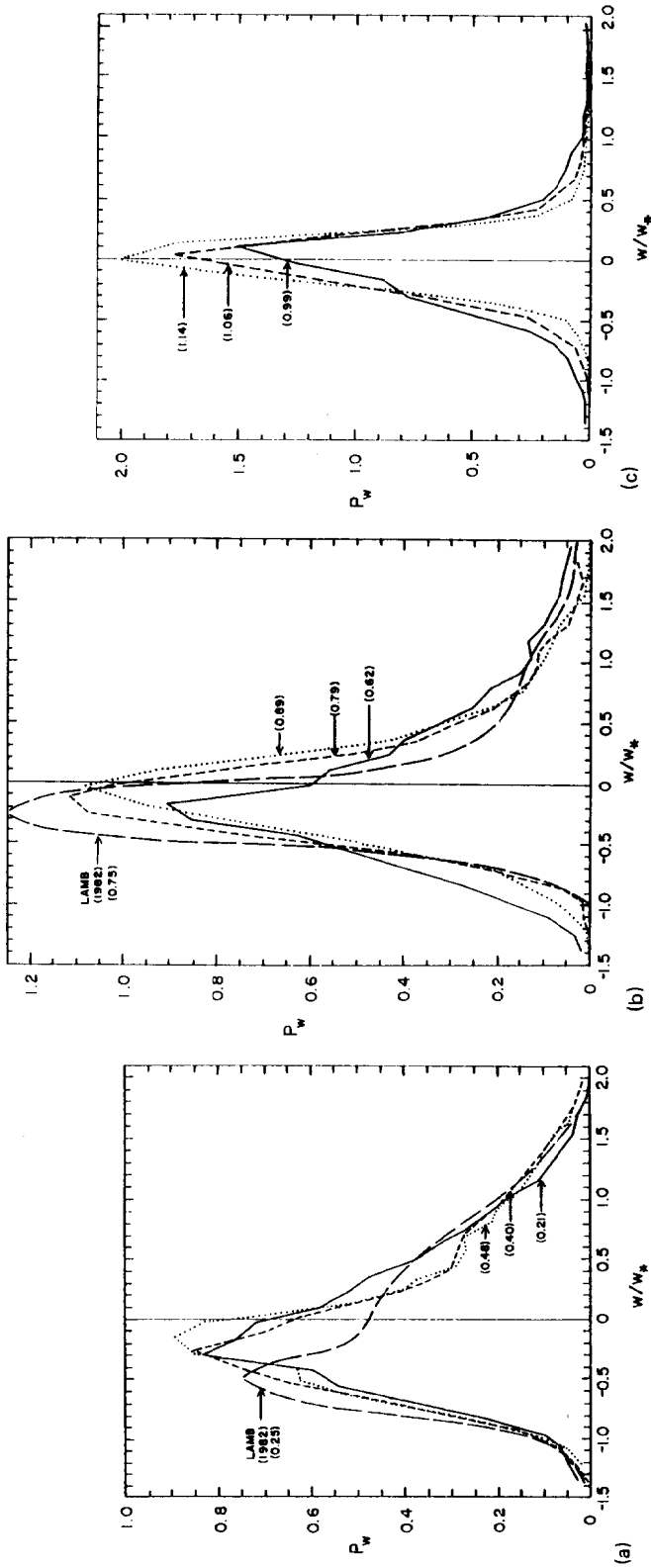


Fig. 16. Vertical-velocity probability distributions,  $R_w$ , versus  $w/w_*$  for  $z/h$  values of: (a) 0.21, 0.40 and 0.48; (b) 0.62, 0.79 and 0.89; and (c) 0.99, 1.06 and 1.14.



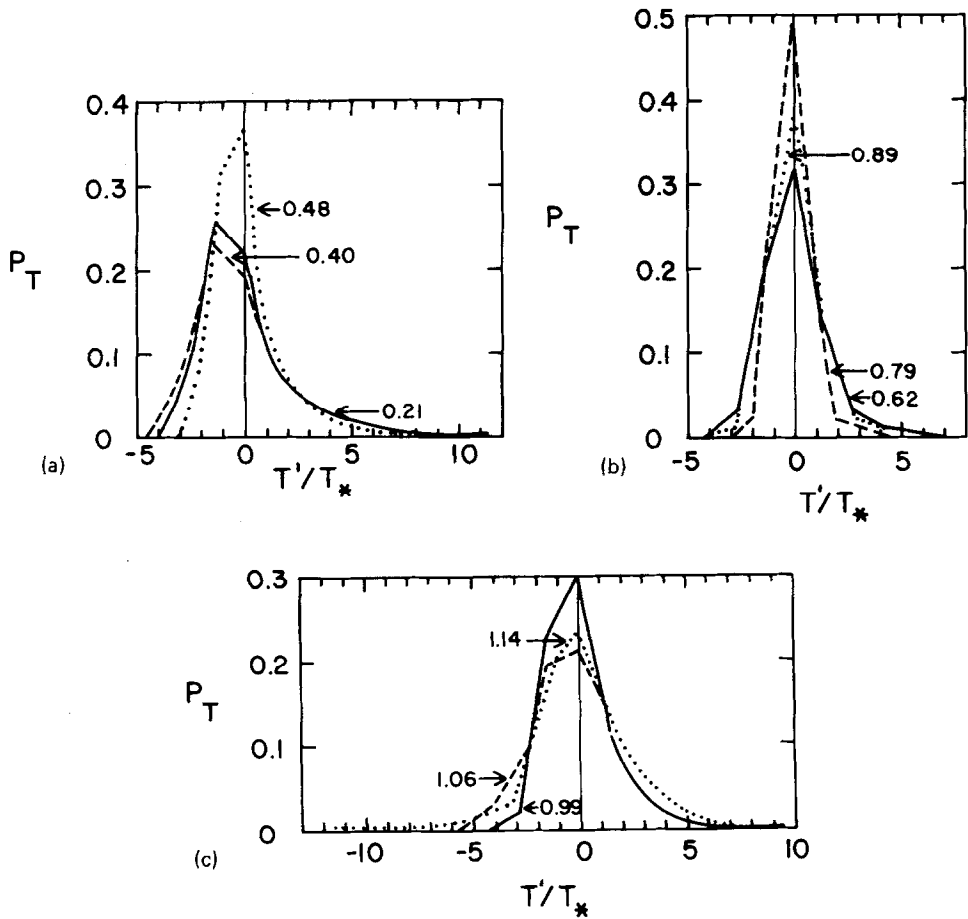
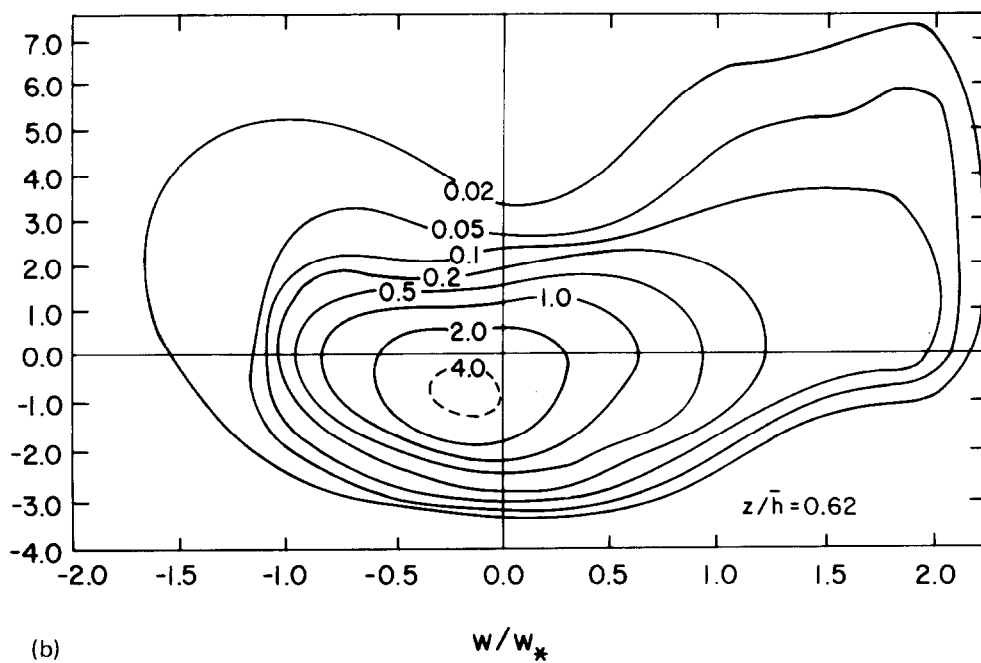
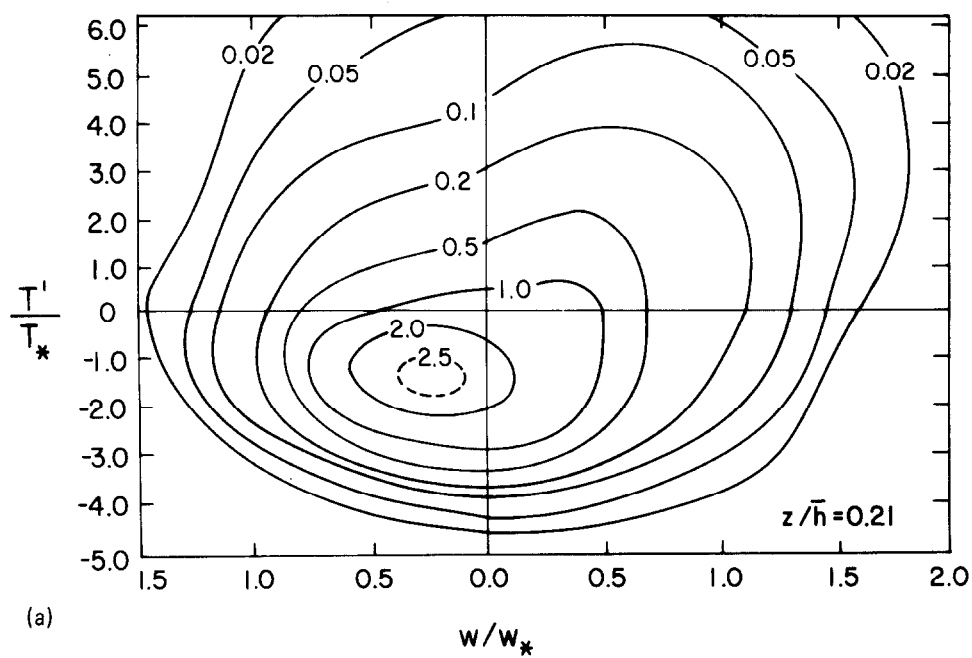
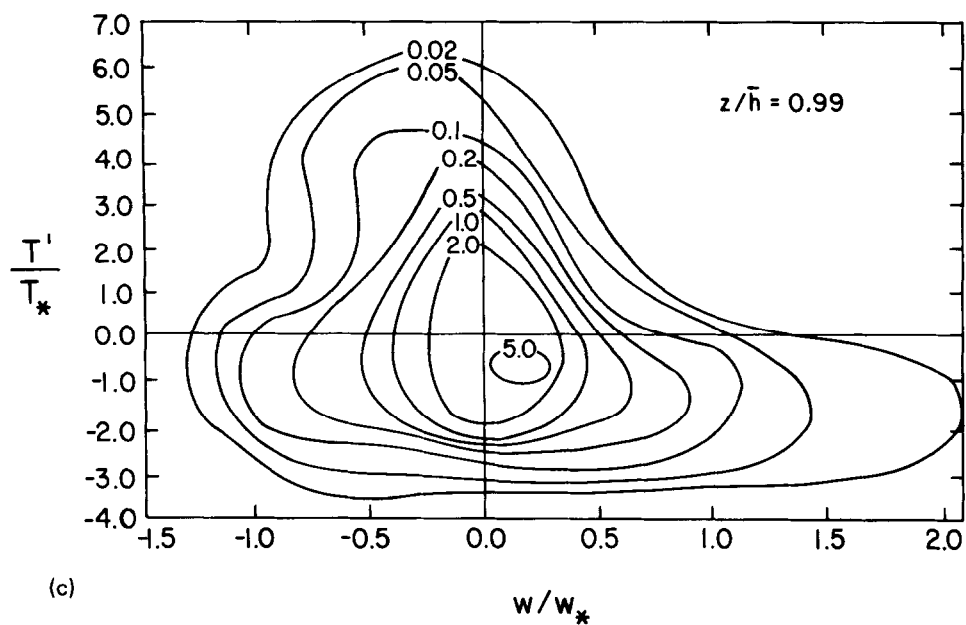


Fig. 17. Temperature-fluctuation probability distributions,  $P_T$ , versus  $T'/T_*$ . See also Figure 16 caption.

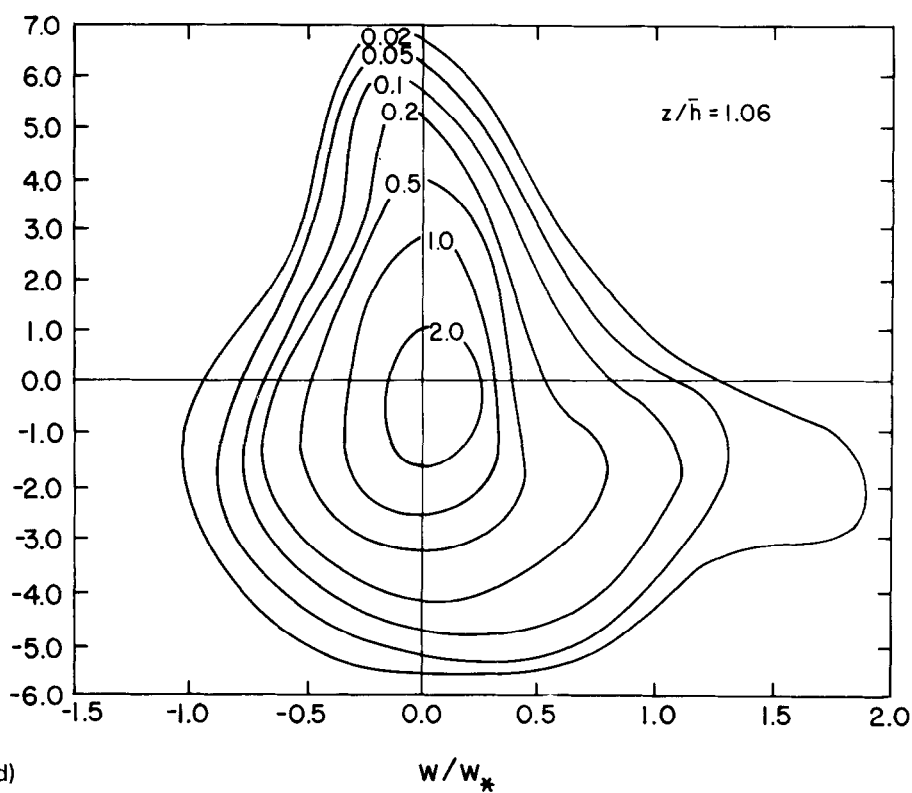
$z/\bar{h} = 0.5$ , they closely resemble  $P_w$ , but their skewness decays more quickly with height. At the greatest height 1.14, extended tails occur, indicative of a large kurtosis.

The joint probability distribution,  $P_{wT}$ , between  $w$  and  $T'$  is shown in Figure 18 for 4 heights. (They are normalized such that  $\int_{-\infty}^{\infty} \int_{-\infty}^{\infty} P_{wT}/(w_* T_*) dw dT' = 1$ .) Figure 18(a, b) show the joint skewness associated with positive heat flux, diminishing with height. Figure 18(c) exhibits asymmetry associated with the entrainment flux, upon noting the prominence of the upper left quadrant where  $w < 0$  and  $T' > 0$ . The same has previously been shown, for example, by Mahrt and Paumier (1984). The lower right quadrant at the same height apparently shows the effect of upward-moving cold domes. At the still greater height of 1.06, Figure 18(d) still exhibits the effects of upward-moving cold domes but not the direct entrainment effect.





(c)



(d)

Fig. 18. Contours of the joint probability distributions,  $P_{wT}$ , versus  $w/w_*$  and  $T'/T_*$ , for  $z/\bar{h}$  of (a) 0.21; (b) 0.62; (c) 0.99; and (d) 1.06. The contours have been smoothed from the original data.

### 3.9. THE ENTRAINMENT RATE

One of the reasons this study emphasizes turbulence measurements in the uppermost 20% of the mixed-layer is so that length, velocity and temperature scales associated with the entrainment can be investigated. One limitation, however, is that only one initial condition was employed in all experiments, in order to maximize the number of observations for a given set of conditions and minimize sampling error. Consequently, only a narrow range of different stabilities at the top of the mixed-layer was encountered, and a rather narrow range in the entrainment rate,  $w_e$ . From each experiment, smooth curves of  $\langle h \rangle(t)$  were drawn, utilizing the spread laser-beam measurements, and values of  $w_e = \partial \langle h \rangle / \partial t$  were taken at approximate times after initiation of convection of 250, 450, and 750s.

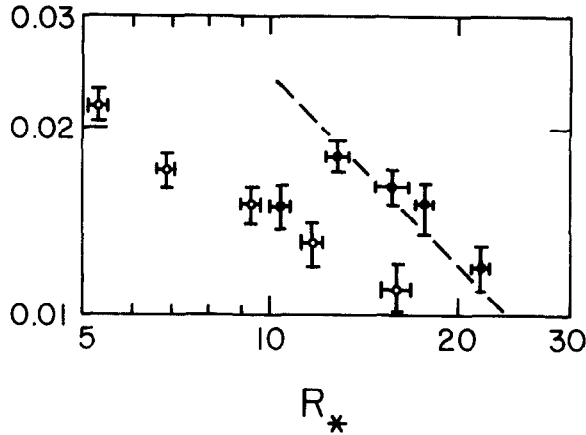


Fig. 19. Entrainment rate,  $w_e$ , normalized by  $w_*$ , versus the stability variable  $R_* = g\beta\Delta T \bar{h}/w_*^2$ . Open circle data points:  $\Delta T$  from  $T^+(\bar{h}) - T_m$  as in (18); closed-circle data points:  $\Delta T$  from  $T(h_2) - T_m$ . Error bars are standard errors of the mean, as opposed to the considerably larger standard deviations about the mean.

With the data grouped into five bunches, the entrainment rate normalized by  $w_*$  is shown in Figure 19 plotted against the stability parameter  $R_{*2}$ , where

$$R_{*2} = g\beta\Delta T_2 \bar{h}/w_*^2 \quad (16)$$

and  $\Delta T_2 = T(\bar{h}_2) - T_m$  (see Section 2) as in Deardorff *et al.* (1980). In 4 of 5 data bunches, the mean  $w_e/w_*$  lies quite close to the mean curve recommended by Deardorff *et al.* (1980, where their  $R_*$  is  $R_{*2}$  here), though the fifth inexplicably does not. This line is the simple relation

$$w_e/w_* = 0.24R_{*2}^{-1}. \quad (17)$$

However, a more sensible definition of  $\Delta T$  is

$$\Delta T = T^+(\bar{h}) - T_m \quad (18)$$

where  $T^+(h)$  is the downward extrapolated (potential) temperature from above the mixed-layer to the height  $\bar{h}$ , as in Smedman and Högström (1983). An equivalent definition which can be used in the laboratory is the initial temperature at  $z = \bar{h}(t)$  minus  $T_m(t)$ . Either of these latter two definitions seems preferable because scarcely any entrainment actually occurs at the height  $z = h_2$ ; instead it is centered at  $z = \bar{h}$ , and the average temperature of the entraining fluid is thus  $T^+(\bar{h})$ . The two different  $\Delta T$ 's become the same if the upper fluid is adiabatic, or non-stratified.

Using the modified stability variable,  $R_*$ , defined by

$$R_* = g\beta\Delta T\bar{h}/w_*^2, \quad (19)$$

the normalized entrainment is shown in Figure 19 by the circles with error bars. Values are shifted to the left because of the smaller  $\Delta T$ 's, and a line of good fit would be  $w_e/w_* = 0.055R_*^{-0.58}$ . However, such a shallow decline rate with  $R_*$  seems unlikely and perhaps an artifice of the mere factor-of-three range in  $R_*$ .

Now, there is some interest in relating the entrainment rate to length and velocity scales actually existing at the level of entrainment itself, just as the temperature stability scale,  $\Delta T$ , applies there. For example, see Turner (1973) and Deardorff and Yoon (1984). Thus, in place of  $\bar{h}$  in (19), one could use  $\sigma_u$  evaluated at  $\bar{h}$ , or  $\sigma_w$  evaluated at  $h_0$ , or  $\Delta h$ , where the latter is essentially the full thickness of the entrainment zone, estimated as  $\Delta h = 1.6(h_2 - \bar{h})$ . For a root-mean-square velocity scale ( $\sigma$ ), one could use  $(\sigma_w)_0$  or  $(\sigma_u)\bar{h}$ , where subscript zero refers to the lower edge of the entrainment zone assumed located at  $\bar{h} - 0.6(h_2 - \bar{h})$ . In Figure 20,  $w_e$  scaled by  $\sigma_u$  with  $R$  containing  $\sigma_u^2$  and  $l_u$  is shown by the triangles. When scaled by  $\sigma_w$  with  $R$  containing  $\sigma_w^2$  and  $l_w$  or  $\Delta h$ , the values are denoted by circles and x's, respectively. The  $\Delta T$ 's from (18) were used. The values and trends seen in Figure 20 using the three different scalings give similar results, indicating only that  $\sigma_u$  tended to be about  $1.13\sigma_w$  at the respective heights of evaluation,  $l_u$  tended to be about  $1.65l_w$ , and  $\Delta h$  was about  $1.4l_w$ . Using the  $\sigma_w$  and  $\Delta h$  scaling, the scaled entrainment rates lie only some 35% below the similarly scaled values of Deardorff and Yoon (1984) associated with shear-induced turbulent entrain-

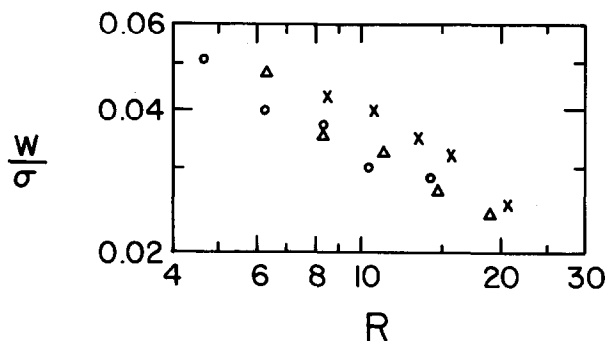


Fig. 20.  $w_e$  normalized by an r.m.s. velocity fluctuation ( $\sigma$ ) versus stability parameter,  $R$ . For  $\circ$  data points,  $\sigma = \sigma_u(\bar{h})$  and  $R = g\beta\Delta T l_u/\sigma_u^2$ . For  $\Delta$  data points,  $\sigma = \sigma_w(h_0)$  and  $R = g\beta\Delta T l_w/\sigma_w^2$ . For  $x$  data points  $\sigma = \sigma_w(h_0)$  and  $R = g\beta\Delta T \Delta h/\sigma_w^2$ . In all three cases  $\Delta T$  is from (18).

ment. Using the  $\sigma_u$  and  $l_u$  scaling, the scaled entrainment lies some 45% below the values of Turner (1973) but above those of Deardorff and Yoon (1984). Turner's (1973) data were for oscillating-grid generated turbulence.

These scaled entrainment rates give a good indication of the magnitudes to be expected using different scaling variables, for  $R_*$  or  $R$  of order 5 to 20, but the rates probably cannot be safely extended over a greater range of stability.

#### 4. Summary and Conclusions

The present results fill in several gaps in our previous laboratory study (W&D) of convective mixed-layer turbulence. They confirm that improved turbulence intensities can be achieved by restricting mixed-layer depths relative to the tank sidewall spacing, but that a convection tank of much greater size would be needed to model an extended inertial subrange. Nevertheless, the short inertial subrange present helped allow fair estimates of dissipation rate to be made, and a reasonable turbulent kinetic energy balance to be achieved. In this budget the most unknown term, convergence of the vertical transport of the pressure fluctuations, tended to offset about half of the convergence of the vertical transport of turbulence.

From the autocorrelation curves, horizontal length scales were presented as a function of height. The  $1/e$  autocorrelation fall-off scales were then used to estimate the proportionality constant in the usual parameterization for the dissipation rate, and in scaling the entrainment rate using local variables.

The individual probability distributions for vertical velocity and temperature showed how the skewness decays with height. Their joint distribution furthermore exhibited effects of entrainment and penetrative convection in the upper mixed-layer.

#### Acknowledgments

The authors acknowledge the indispensable help of P. Stockton in developing and maintaining the measurement systems utilized, and in aiding during experiments. We also thank graduate student J.-W. Kim for aiding during experiments and for performing much data analysis. The work was supported by the National Science Foundation, Meteorology Section, under Grant ATM 80-19778, and also by the Office of Naval Research.

#### References

- Adrian, R. J. and Ferreira, R. T. S.: 1979, 'Higher Order Moments in Turbulent Thermal Convection', *2nd Symposium on Turbulent Shear Flows*, July 2-4, Imperial College, London, 12.1-12.5.
- Andreas, E. L.: 1979, 'Analysis of Crossed Hot-Film Velocity Data', *DISA Information* **24**, 15-23.
- Batchelor, G. K.: 1959, 'Small-scale Variations of Convected Quantities like Temperature in Turbulent Fluid. Part 1. General Discussion and Case of Small Conductivity', *J. Fluid Mech.* **5**, 113-133.
- Caughey, S. J.: 1982, 'Observed Characteristics of the Atmospheric Boundary Layer', in *Atmos. Turbulence and Air Pollution Modelling*, D. Reidel, Dordrecht, pp. 107-156.

- Caughey, S. J. and Wyngaard, J. C.: 1979, 'The Turbulence Kinetic Energy Budget in Convective Conditions', *Quart. J. Roy. Meteorol. Soc.* **105**, 231–239.
- Caughey, S. J., Kitchen, M., and Leighton, J. R.: 1983, 'Turbulence Structure in Convective Boundary Layers and Implications for Diffusion', *Boundary-Layer Meteorol.* **25**, 345–352.
- Champagne, F. H., Sleicher, C. A., and Wehrmann, O. H.: 1967, 'Turbulence Measurements with Inclined Hot-Wires', *J. Fluid Mech.* **28**, 153–176.
- Deardorff, J. W.: 1979, 'Prediction of Convective Mixed-Layer Entrainment for Realistic Capping Inversion Structure', *J. Atmos. Sci.* **36**, 424–436.
- Deardorff, J. W., and Willis, G. E.: 1982, 'Investigation of the Frozen-Turbulence Hypothesis for Temperature Spectra in a Convectively Mixed Layer', *Phys. Fluids* **25**, 21–28.
- Deardorff, J. W. and Willis, G. E.: 1984, 'Groundlevel Concentration Fluctuations from a Buoyant and a Non-Buoyant Source within a Laboratory Convectively Mixed Layer', *Atmos. Envir.* **18**, 1297–1309.
- Deardorff, J. W. and Yoon, S.-C.: 1984, 'On the Use of an Annulus to Study Mixed-Layer Entrainment', *J. Fluid Mech.* **141**.
- Deardorff, J. W., Willis, G. E., and Lilly, D. K.: 1969, 'Laboratory Investigation of Non-Steady Penetrative Convection', *J. Fluid Mech.* **35**, 7–31.
- Deardorff, J. W., Willis, G. E., and Stockton, B. H.: 1980, 'Laboratory Studies of the Entrainment Zone of a Convectively Mixed Layer', *J. Fluid Mech.* **100**, 41–64.
- Dickey, T. D. and Mellor, G. L.: 1980, 'Decaying Turbulence in Neutral and Stratified Fluids', *J. Fluid Mech.* **99**, 13–31.
- Druihet, A. and Durand, P.: 1984, 'Etude de la Couche Limite Convective Sahelienne en Presence de Brumes Seches (Experience ECLATS)', *Boundary-Layer Meteorol.* **28**, 51–78.
- Ferreira, R. T. de S.: 1978, 'Unsteady Turbulent Thermal Convection', Ph.D. Thesis, Dept. of Mech. Egn., University of Illinois, Urbana, Ill, 225 pp.
- Grant, H. L., Hughes, B. A., Vogel, W. M., and Moilliet, A.: 1968, 'The Spectrum of Temperature Fluctuations in Turbulent Flow', *J. Fluid Mech.* **34**, 423–442.
- Grossman, R. L.: 1982, 'An Analysis of Vertical Velocity Spectra Obtained in the BOMEX Fair-Weather, Trade-Wind Boundary Layer', *Boundary-Layer Meteorol.* **23**, 323–357.
- Guillemet, B. G., Isaka, H., and Mascart, P.: 1983, 'Molecular Dissipation of Turbulent Fluctuations in the Convective Mixed Layer, Part 1: Height Variations of Dissipation Rates', *Boundary-Layer Meteorol.* **27**, 141–162.
- Hassid, S. and Galperin, B.: 1983, 'A Turbulent Energy Model for Geophysical Flows', *Boundary-Layer Meteorol.* **26**, 397–412.
- Ivanov, V. N.: 1970, 'The Use of the Tall IEM Meteorological Tower for the Study of the Boundary Layer of the Atmosphere', *Gidrometizdat* Moscow, 143 pp. (in Russian).
- Kaimal, J. C., Wyngaard, J. C., Haugen, D. A., Coté, O. R., Izumi, Y., Caughey, S. J., and Readings, C. J.: 1976, 'Turbulence Structure in the Convective Boundary Layer', *J. Atmos. Sci.* **33**, 2151–2169.
- Lamb, R. G.: 1982, 'Diffusion in the Convective Boundary Layer', in *Atmospheric Turbulence and Air Pollution Modelling*, D. Reidel, Dordrecht, pp. 159–229.
- Lenschow, D. H.: 1970, 'Airplane Measurements of Planetary Boundary Layer Structure', *J. Appl. Meteorol.* **9**, 874–884.
- Lenschow, D. H., Wyngaard, J. C., and Pennell, W. T.: 1980, 'Mean-Field and Second-Moment Budgets in a Baroclinic, Convective Boundary Layer', *J. Atmos. Sci.* **37**, 1313–1326.
- Mahrt, L., and Paumier, J.: 1984, 'Heat Transport in the Atmospheric Boundary Layer', *J. Atmos. Sci.* **41**, 3061–3075.
- Smedman, A.-S. and Högstrom, U.: 1983, 'Turbulent Characteristics of a Shallow Convective Internal Boundary Layer', *Boundary-Layer Meteorol.* **25**, 271–287.
- Taylor, G. I.: 1935, 'Statistical Theory of Turbulence. Part II', *Proc. Roy. Soc.* **A151**, 444–454.
- Townsend, A. A.: 1964, 'Natural Convection in Water over an Ice Surface', *Quart. J. Roy. Meteorol. Soc.* **90**, 248–259.
- Turner, J. S.: 1973, *'Buoyancy Effects in Fluids'*, Cambridge University Press, 367 pp.
- Willis, G. E. and Deardorff, J. W.: 1974, 'A Laboratory Model of the Unstable Planetary Boundary Layer', *J. Atmos. Sci.* **31**, 1297–1307.
- Willis, G. E., and Deardorff, J. W.: 1976, 'A Laboratory Model of Diffusion into the Convective Planetary Boundary Layer', *Quart. J. Roy. Meteorol. Soc.* **102**, 427–445.

- Willis, G. E. and Deardorff, J. W.: 1981, 'A Laboratory Study of Dispersion from a Source in the Middle of the Convectively Mixed Layer', *Atmos. Envir.* **15**, 109–117.
- Wyngaard, J. C. and LeMone, M. A.: 1980, 'Behavior of the Refractive Index Structure Parameter in the Entraining Convective Boundary Layer', *J. Atmos. Sci.* **37**, 1574–1585.
- Wyngaard, J. C., Coté, O. R., and Izumi, Y.: 1971, 'Local Free Convection, Similarity, and the Budgets of Shear Stress and Heat Flux', *J. Atmos. Sci.* **28**, 1171–1182.
- Zeman, O. and Tennekes, H.: 1977, 'Parameterization of the Turbulent Energy Budget at the Top of the Daytime Atmospheric Boundary Layer', *J. Atmos. Sci.* **34**, 111–123.